ChemComm
Chemical Communications

Accepted Manuscript

This article can be cited before page numbers have been issued, to do this please use: Z. Shi, X. Lai, C. Sun, X. Zhang, L. Zhang, Z. Pu, R. Wang, H. Yu and D. Li, *Chem. Commun.*, 2020, DOI: 10.1039/D0CC03628E.

View Article Online
DOI: 10.1039/D0CC03628E

ARTICLE

Step emulsification in microfluidic droplet generation: mechanisms and structures

Received 00th January 20xx,
Accepted 00th January 20xx

DOI: 10.1039/x0xx00000x

Zhi Shi,[a] Xiaochen Lai,[a] Chengtao Sun,[a] Xingguo Zhang,[a] Lei Zhang,[a] Zhihua Pu,[a] Ridong Wang,[a] Haixia Yu[b] and Dachao Li*[a]

The Droplet-based microfluidic techniques have been applied widely in functional material synthesis and biomedical information measurements, wherein step emulsification is an integrated system that combines the advantages of homogeneity and throughput in monodisperse droplet formation. This paper reviews the mechanisms and classical structures of step emulsification. In terms of droplet formation mechanisms, we describe the droplet size and detachment regimes related to the microchannel geometry. Distinguished by droplet formation, microfluidic step emulsification driven by interfacial tension and centrifugal step emulsification related to buoyancy are introduced. In addition, the improved structures for enhancing the droplet homogeneity and throughput are described in this paper as well. Finally, the perspectives about the developments of step emulsification in mechanisms, fabrications, and applications are discussed.

1. Introduction

Emulsification merges immiscible fluids into mass-independent reaction units, which have been attributed to many applications, such as food production, materials synthesis, and biomedical science[1-5]. As microscale templates, emulsion droplets are used in functional material synthesis, such as microparticles[6-9] and microcapsules[10, 11], which are revolutionizing drug delivery[12, 13]. As ideal chemical and biological microreactors, emulsion droplets within nanolitre and picolitre volumes have been applied in digital assays for single-molecule detection[14-16], such as digital polymerase chain reaction[17, 18], single-cell analysis[19, 20], enzyme analysis[21, 22], and genome sequencing[23, 24].

There are active and passive methods in emulsion droplet generation. In passive methods, droplet formation depends on the intrinsic properties of fluids. The detachment regimes of droplets are dominated by the competition of capillary, viscous and inertial forces. In active methods, droplet formation is dominated by external forces, such as electrical, magnetic, centrifugal, optical, thermal, and mechanical forces[25]. For microfluidic structures of droplet generation, it is common that the viscous shear force affects droplet detachment. The cross-flow[26-30], co-flow[31-33], and flow-focusing[34-37] techniques are representative among these methods. However, in these emulsifications the size and homogeneity of droplets depend severely on the flow rate of fluids. Then, mass monodisperse droplet production is limited in these ways since slight fluctuations in the flow rate will result in polydisperse droplets. Moreover, another disadvantage of such methods is the dead volume, which inevitably leads to sample waste. Generating uniform droplets by variations of channel confinement, step emulsification[38-41] is extensively used in both research and applications. The size of the emulsion droplet is exclusively dominated by the geometry of devices and is independent of the flow rates of fluids in the dripping regime. In addition, the dead volume would be eliminated by optimizing the experimental workflow. The throughput of emulsification could be improved by adjusting the critical velocity and parallelization of the droplet formation units. Such advantages have promoted step emulsification to be applied in the mass production of monodisperse droplets with high efficiency.

In this paper, we review the mechanisms for droplet formation and various microfluidic structures of step emulsification. First, we introduce a quasi-static mechanism for droplet formation, after which the influences of the droplet size and droplet detachment regimes from the structure geometry are illustrated. Second, the microchannels step emulsification structures in which droplet formation is dominated by interfacial tension are introduced, including the grooved-type microchannel, the straight-through microchannel, the edge-based droplet generation device, the triangular nozzle microchannel and their improved structures for droplet homogeneity and throughput. Third, as integrated platforms for digital assays, the devices of centrifugal step emulsification in which droplet formation is dominated by interfacial tension and buoyancy produced by the centrifugal field are depicted in this paper. Finally, the critical commentary about the structure flexibility of step emulsification is statemented, and further developments are considered based on the mechanism, fabrication, and application.

[a] State Key Laboratory of Precision Measuring Technology and Instruments, Tianjin University, Tianjin, 300072, China. E-mail: dchli@tju.edu.cn
[b] Tianjin Key Laboratory of Biomedical Detecting Techniques and Instruments, Tianjin University, Tianjin, 300072, China

View Article Online
DOI: 10.1039/D0CC03628E

2. Mechanism of step emulsification

2.1 A quasi-static mechanism for droplet formation

Microfluidic step emulsification is used to generate droplets with diameters ranging from nanometres to hundreds of micrometres. The main components of microfluidic step emulsification consist of a dispersed phase channel, a reservoir of the continuous phase and a nozzle, with a height that is significantly different from the reservoir. The schematic is illustrated in Fig. 1a. After microchannel emulsification for droplet formation was first presented[38], most of the research on the droplet formation mechanism are based on experimental phenomena[42, 43] and numerical simulations[39, 44, 45]. Afterwards, geometric models[46] were presented to characterize the process of step emulsification. Among the reported physical mechanisms, a quasi-static mechanism related to the structure geometry has been proposed to explain droplet formation[47, 48].

The quasi-static mechanism is based on three hypotheses[47]. The first condition is that the dispersed phase cannot wet the channel walls for droplet formation. The second condition is to neglect the gravitational effect. The third condition is that the system evolves in a quasi-static manner. The Young-Laplace equation is used to contact the mean curvature κ with the pressure of the outer phase p_o and inner phase p_i,

$$\gamma\kappa = p_i - p_o \quad (1)$$

where the mean curvature κ is the sum of curvatures of the surface along with its two principal directions. When the flow pressure fluctuations are negligible compared with the Laplace jump $\gamma\kappa$, the mean curvature κ is constant over the interface. The quasi-static hypothesis implies that the mean curvature matches between the thread upstream of the step and the blub downstream of the step in an equilibrium state.

In the quasi-static mechanism of step emulsification, the continuous phase with surfactant is filled into the reservoir in advance, and the immiscible dispersed phase is injected into the channel (Fig. 1.b.I). When the thread of the dispersed phase crosses the step, a blub emerges downstream of the step. As the sustained injection of the dispersed phase, the mean curvature of the blub decreases, while its size increases. To match the mean curvature of the bulb, the mean curvature of the thread decreases until it reaches the critical value $2/h$ caused by the confinement of the nozzle channel (Fig. 1.b.II). After that, the equilibrium is broken because the thread could no longer match the reduction of the blub mean curvature. A necking region appears between the thread and the bulb and then grows in time during disequilibrium. The cross-section length of the neck w_n decreases as the necking region grows. When w_n decreases to nozzle height h, the bulb detaches from the thread of the dispersed phase caused by the Rayleigh-Plateau instability[49] (Fig. 1.b.III). Eventually, a droplet is released into the continuous phase and the thread shrinks back to the nozzle for the next droplet formation (Fig. 1.b.IV). The necking time depends on the viscosity ratio and interfacial tension[50], during which the backflow of the continuous phase contributes to the expansion of the necking region[51].

2.2 Structure geometry

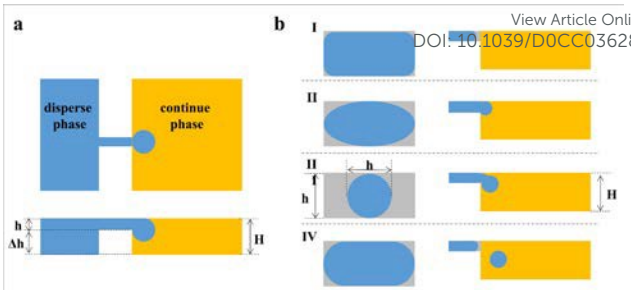

Fig. 1 Schematic of step emulsification. (a) Top and side views of the step emulsification structure. (b) Cross-sectional views of the nozzle in two lateral directions. I. The dispersed phase is injected into the nozzle; II. The radius of bulb reaches the critical value and begins to form the necking region; III. The diameter of the neck decreases to the nozzle height after necking; IV. The droplet detaches from the dispersed phase into the continuous phase.

Microchannel step emulsification is driven by interfacial tension[52], and the size of the droplet is primarily dominated by the geometry of the microchannel. A grooved-type microchannel was proposed initially[38] whose structure is illuminated in Fig. 2a. There is a terrace between the nozzle and the continuous phase reservoir. After the dispersed phase is injected, the thread goes through the nozzle and inflates over the terrace. Under the step emulsification mechanism, the bulb increases gradually and detaches into a droplet by the Rayleigh-Plateau instability. The effect of nozzle length on the droplet diameter is measured by maintaining a constant nozzle width, depth, and terrace length. Similarly, the relationship between droplet diameter and nozzle width has been studied. The results reveal that the droplet diameter is independent of both the nozzle length and width[43].

The nozzle depth is a dominant parameter with respect to the droplet size in step emulsification, and the terrace length has a slight influence as well. The geometry of the nozzle is controlled to characterize the influence of the terrace length on the droplet size[42]. The droplet diameter increases slightly with increasing terrace length; however, the detachment length defined as the distance between the terrace end and the position where the droplet detaches is constant regardless of the terrace length. The experiments of structures with different nozzle heights reveal that the droplet diameter is linearly related to the nozzle height. Supposing that the thread is disk-shaped over the terrace before droplet detaching, the final volume of the droplet is a function of the detachment length A and structure geometry.

$$V = H\left[\frac{L^2\phi}{4} - \frac{L(L-2A)}{4}\sin\phi\right] \quad (2)$$

where H is the nozzle height, L is the terrace length and the angle ϕ is defined as:

$$\cos\phi = \frac{L-2A}{L} \quad (3)$$

The diameter of a droplet can be computed by:

$$D = \left(\frac{6V}{\pi}\right)^{1/3} = \left(\frac{6H}{\pi}\left(\frac{L^2}{4}\cos^{-1}\left(\frac{L-2A}{L}\right) - \frac{L(L-2A)}{4}\sin\left(\cos^{-1}\left(\frac{L-2A}{L}\right)\right)\right)\right)^{1/3} \quad (4)$$

It is necessary to point out that the above analysis is effective in the dripping regime which is discussed in the following sections. Furthermore, the numerical relationship between droplet diameter and nozzle height could be computed by regression

View Article Online
DOI: 10.1039/D0CC03628E

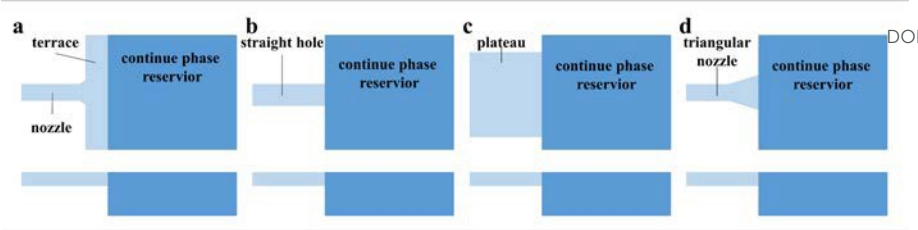

Fig. 2 Schematics of microfluidic step emulsification devices. (a) The grooved-type microchannel. (b) The straight-through microchannel. (c) The edge-based droplet generation (EDGE) device. (d) The triangular nozzle microchannel.

analysis with experimental data, and is useful for modifying the droplet diameter prediction[42].

Corresponding with the flow rate of the dispersed phase, the dimensionless parameter Capillary number *Ca* is used to characterize the dripping regime and jetting regime of droplet formation. In the dripping regime, the droplet size is insensitive to the input flow rate, and in the jetting regime, the droplet size increases significantly with increasing flow rate. Capillary number *Ca* is the ratio of the viscosity force to the interfacial tension:

$$Ca = \frac{\eta_{\mathrm{dis}} U}{\gamma} \quad (5)$$

where η_{dis} is the viscosity of the dispersed phase, γ is the interfacial tension between two phases and U is the characteristic flow rate of the dispersed phase. There is a critical Capillary number *Ca** distinguishing the two regimes of droplet formation. When Capillary number is below *Ca**, emulsification is dominated by the interfacial tension, and the dispersed phase forms monodisperse droplets spontaneously in the dripping regime. While Capillary number is larger than *Ca**, emulsification is dominated by the viscosity force, and polydisperse droplets are produced in the jetting regime. The critical Capillary number represents the range of monodisperse droplet formation in the dripping regime, and the mass production of monodisperse droplets is easier to achieve with a higher *Ca**. The critical Capillary number is related to the structure geometry, a higher critical Capillary number can be obtained through a longer or narrower nozzle[43]. Furthermore, the critical Capillary number is independent of neither the viscosity of the fluid nor the nozzle height for a constant viscosity ratio of two phases[53].

Moreover, the fluid properties have been studied in step emulsification. As a force driving droplet formation, the interfacial tension is irrelevant to the droplet size, although it influences the temporal characteristics of droplet formation[54]. Except for experiments, computational fluid dynamics (CFD) simulations have always been used to characterize the numerical relationships between the physical parameters and emulsification[45, 55, 56]. The viscosity ratio is an important parameter for the droplet formation regimes, and a minimum and a critical viscosity ratio are found in the microchannel step emulsification[57]. When the viscosity ratio of the dispersed and continuous phases is higher than the critical viscosity ratio, the droplet size is constant. The droplet diameter increases as the viscosity ratio decreases until the minimum viscosity ratio is reached, below which the droplet cannot be emulsified[57-59]. As well as the critical Capillary number, the minimum and critical viscosity ratio could be adjusted by the geometry of microchannel structures. For a grooved-type microchannel, a shorter terrace and longer nozzle would lead to a lower critical and minimum viscosity ratio[57]. A CFD simulation has been established for investigating the influence of the wall contact angle on the droplet diameter in step emulsification, and the droplet diameter increases as the contact angle decreases[60]. Furthermore, the introduction of a continuous phase co-flow mechanism[61] in step emulsification could broaden the ranges of wall contact angle for droplet formation from 140°-180° to 90°-180°[62].

3. Microfluidic step emulsification

The interfacial tension dominates droplet formation in a microchannel step emulsification driven by the pressure or flow rate, where the gravity effect is always neglected. The grooved-type microchannel consists of a dispersed phase channel, a nozzle, a terrace and a continuous phase reservoir as depicted in Fig. 2a. There is a height difference between the terrace and reservoir for step emulsification. The device is manufactured on a silicon wafer by photolithography and orientation-dependent etching[43], as shown in Fig. 3. To generate monodisperse droplets in the dripping regime, the continuous phase is injected into the microchannel first to wet the walls and be full of the reservoir; then, the dispersed phase is driven by the pressure or flow rate under the critical Capillary number. The droplet diameter is linear with the nozzle height with a factor of approximately 4. The influences of the droplet size and formation regimes by the fluid properties and driven parameters are depicted in section 2.

A straight-through microchannel is proposed for step emulsification, the structure of which includes exclusively elongated straight holes for droplet formation[63, 64], as shown in

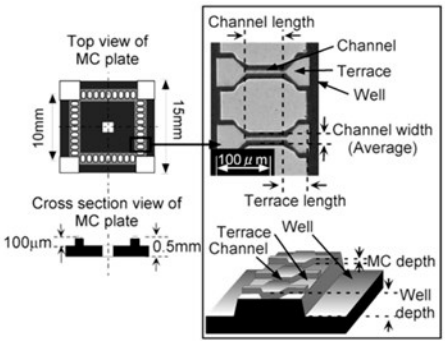

Fig. 3 Schematic of silicon grooved-type microchannel. Reprinted with permission from ref. 43. Copyright (2002) American Chemical Society.

View Article Online
DOI: 10.1039/D0CC03685E

Fig. 2b. Deep reactive ion etching (DRIE) on a silicon wafer is used to fabricate the device. Except for a closed channel, a continuous phase could be placed in an open reservoir, and the dispersed phase is driven into the straight hole to detach the droplets at the exit, as shown in Fig. 4a. The droplet diameter is linearly related to the depth of the straight hole, which is roughly a multiple of 4. There is a critical aspect ratio of approximately 3-3.5, below which droplet detachment requires a strong backflow of the continuous phase， and the droplet size is so unstable that a continuous outflow emerges. In contrast, when the straight hole aspect ratio is above the critical value, monodisperse droplets are generated spontaneously in the dripping regime[55, 65]. Similar to the grooved type, the critical Capillary number corresponding to the flow rate is a boundary between the dripping and jetting regimes[51]. The critical Capillary number is related to the viscosity ratio of two phases, and the critical Capillary number could be improved by providing the continuous phase with high interfacial tension[66]. Throughput enhancement of droplet formation could be realized by both the critical Capillary number adjustment and straight hole parallelization. The simple structure of a straight hole is suitable for parallel fabrication, as shown in Fig. 4b, and high-throughput monodisperse droplet generators are generally made in an open reservoir with arrayed straight holes.

The parallel straight-through microchannel for high throughput is confronted with droplet congestion out of the nozzle, which hinders the homogeneity and productivity of droplet formation. A step emulsification device applying the buoyancy to clear formed droplets out of the nozzle spontaneously without a shear flow has been proposed[67], as shown in Fig. 4(c). The device with parallel nozzles is placed in the continuous phase, and the density difference between two phases causes the clearance of droplets as soon as they detach from the nozzles. The master is fabricated by soft lithography for droplet diameters smaller than 300 μm, and a 3D printed master is applied to generate droplets whose diameters are above 300 μm. After pouring polydimethylsiloxane (PDMS) and bonding with a glass plate, the device could produce monodisperse droplets with diameters ranging from 30 to 1000 μm with coefficients of variation (CV) of 3%-5%, and the throughput of droplet formation was up to 10 L/h.

The edge-based droplet generation (EDGE) device is another step emulsification structure for high-throughput droplet formation. Instead of the straight hole, there is a wide shallow plateau as the nozzle, in which it is realized that parallel droplets are generated from a single nozzle simultaneously. The schematic diagram is shown in Fig. 2c. A silicon wafer is patterned by the deep reactive ion etching (DRIE) technique and then bonded with a glass plate[68]. As shown in Fig. 5, compared with a rectangular plateau (Fig. 5a), a triangular plateau (Fig. 5b), the width of whose cross section gradually increases from the dispersed phase channel to the continuous phase reservoir, has a higher critical Capillary number. There is a throughput advantage in the EDGE microchannels by producing parallel droplets through a single nozzle; On the other hand, the CV of approximately 10% is expected to be optimized. To improve the stability of the droplet formation process, partitioned structures are added on the plateau, as shown in Fig. 5c. Although the droplet diameter increases with increasing driving pressure, the CV of the droplet remains below 5% in the pressure range from 115 mbar to 1000 mbar. Compared with the rectangular EDGE device, the partitioned EDGE device has a smaller scaling factor between the droplet diameter and the plateau height, and the scaling factors are 6 and 4.5 respectively. An unexpected phenomenon is that as the driving pressure increases, larger monodisperse droplets with a scaling factor of 14 are generated between 1400 and 2800 mbar[69]. However, the robustness and congestion possibility of the device should be considered during high-throughput droplet generation. Furthermore, it is reported that there is a better insensitivity between the droplet diameter and the variety of input flow rates when the height of the partitioned structure is more than half of the plateau height[70]. Combined with the parallelization and locality of droplet formation, EDGE devices have an

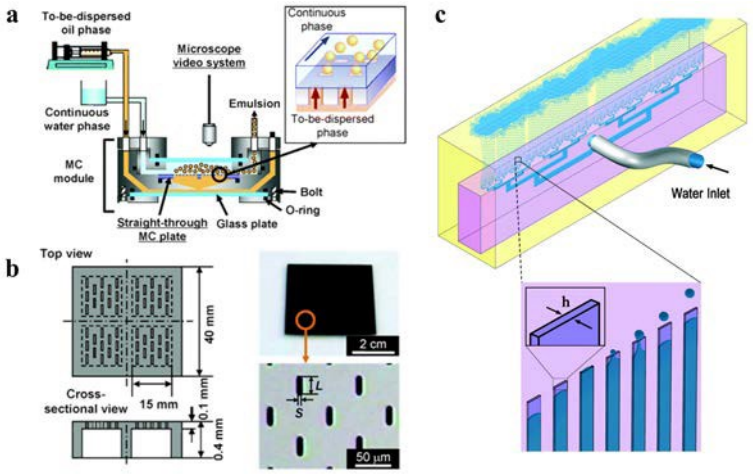

Fig. 4 Schematic of the straight-through microchannel. (a) Schematic of the system for straight-through microchannel emulsification. Reprinted with permission from ref. 66. Copyright (2005) American Chemical Society. (b) Schematic and photograph of a silicon parallel straight holes microchannel. Reprinted with permission from ref. 66. Copyright (2005) American Chemical Society. (c) Parallel step emulsifier devices by shear-free and efficient nozzle clearance. Reproduced from Ref. 67 with permission from The Royal Society of Chemistry.

View Article Online
DOI: 10.1039/D0CC03628E

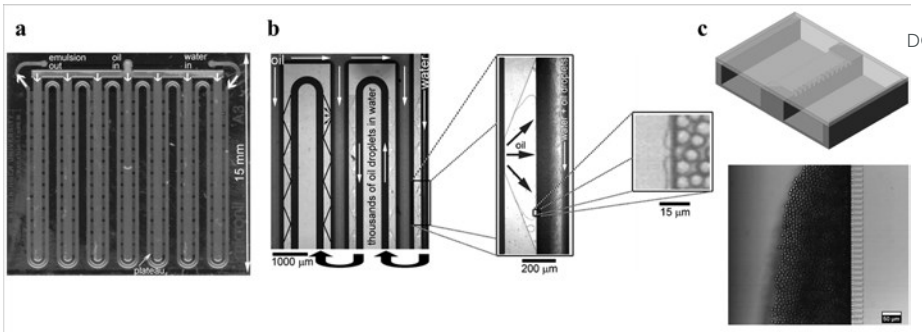

Fig. 5 Schematic of The edge-based droplet generation (EDGE) device. (a) EDGE device with rectangular plateaus. Reproduced from Ref. 68 with permission from The Royal Society of Chemistry. (b) EDGE device with triangular plateaus. Reproduced from Ref. 68 with permission from The Royal Society of Chemistry. (c) Schematic and photograph of the partitioned EDGE device. Reproduced from Ref. 69 with permission from The Royal Society of Chemistry.

inherent advantage with regard to the throughput, and optimizing the structure to ensure the homogeneity of droplets would bring the structures into more applications.

The triangular nozzle microchannel exhibits a more optimized performance for droplet formation than the rectangular nozzle. The triangular nozzle plays the role of the terrace for the backflow of the continuous phase with the stretched cross section, as shown in Fig. 2d. With the inflation of the dispersed phase in a triangular nozzle, there is a gradual Laplace pressure that decreases the flow rate of the thread and decouples the correlation between the local flow rate and the external driven flow rate. The triangular nozzle provides a local independent area for droplet formation to prevent extra interference from both the dispersed and continuous phases. The throughput of droplet formation could be improved by paralleling nozzles along the channels. A millipede device is designed for 20-160 μm diameter monodisperse droplet generation, retaining the throughput up to 150 mL/h with a CV below 3%. As shown in Fig. 6a, this device contains a total of 550 triangular nozzles along both sides of the dispersed phase channel[71]. The master is fabricated by the soft lithography technique on which PDMS is poured to form the microchannel pattern. The diameter of the monodispersed droplet depends on the nozzle height, as in other step emulsification methods; Furthermore, it is essential for the aspect ratio of the nozzle ranging from 5.5 to 19. In the droplet generation regimes, there is a critical Capillary number that distinguishes the jetting regime and dripping regime in which the droplet size is independent of the input flow rate. This kind of step emulsification achieves highly uniform droplet formation while maintaining high throughput and thus has been applied in mass monodisperse droplet production. A glass-based device with 364 parallel triangular nozzles is shown in Fig. 6b. The device whose master is manufactured by wet etching has been exploited in functional material syntheses, such as toluene droplets, polycaprolactone (PCL) microcapsules, magnetically responsive droplets, and poly(N-isopropylacrylamide) (pNIPAm) microspheres[72].

Concerning the parallel nozzle structures, the driving of the continuous phase is necessary to prevent droplet clustering and merging outside the nozzles. In addition, the backflow of the continuous phase is effectual for droplet detachment. The shunt channels have been utilized in the triangular nozzle for enhancing continuous phase backflow[73]. The 3D shunt channel modified triangular nozzle device is illustrated in Fig. 6c, and it is confirmed that the maximum flow rate of the dispersed phase in the dripping regime has been increased significantly without altering the size and size distribution of droplets[74]. Such a 3D shunt channel modified device indeed has an advantage with

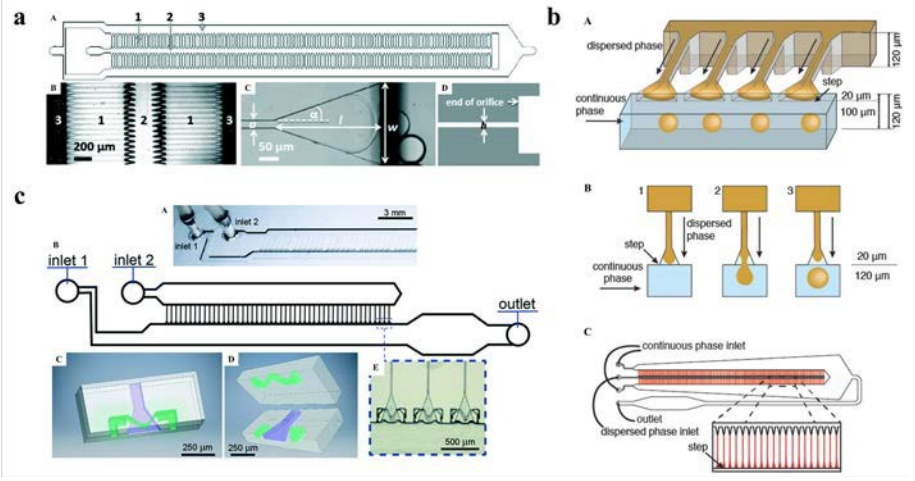

Fig. 6 Schematic of the triangular nozzle microchannel. (a) Schematic illustration of the millipede device with parallelized triangular nozzles. Reproduced from Ref. 71 with permission from The Royal Society of Chemistry. (b) Layout and working principle of a glass microfluidic device for parallelized step emulsification. Reproduced from Ref. 72 with permission from John Wiley and Sons. (c) Shunt channels modified triangular nozzle microchannel. Reproduced from Ref. 74 with permission from The Royal Society of Chemistry.

View Article Online
DOI: 10.1039/D0CC02685E

throughput; however, it is noteworthy that the overlay alignments with multilayer structures significantly increase the difficulty of soft lithography processing, and the obvious polydispersity of droplets would be caused by a misalignment.

4. Centrifugal step emulsification

In the mechanism of centrifugal step emulsification, an artificial gravity field is produced by centrifugal force, resulting in a gravity effect that cannot be neglected. Except for being driven by interfacial tension, droplet detachment is dominated by buoyancy, which is affected by the centrifugal field and the density difference between the dispersed phase and the continuous phase. A dimensionless parameter Bond number is used to describe the balance between the interfacial tension and buoyancy in droplet formation. The definition of Bond number *Bo* is the ratio of buoyancy to the interfacial tension:

$$Bo = \frac{\Delta\rho g H^2}{\gamma} \quad (6)$$

where $\Delta\rho$ is the density difference between the dispersed and continuous phases, γ is the interfacial tension between the two phases, g is the gravitational acceleration which represents the centrifugal acceleration, and H is the characterized height. It is reported that the Bond number is linearly related to the Capillary number in centrifugal step emulsification, and the slope is affected by the flow resistance of microchannels; in detail, a microchannel with a higher flow resistance represents a higher slope between the Bond and Capillary number[75]. Cooperating to influence the regimes of droplet formation, the Bond number and Capillary number each has a critical value. When Capillary number is below the critical value, the monodisperse droplets detach in the dripping regime dominated by the interfacial tension. When Capillary number is above the critical value and Bond number is below its critical value, the generated droplet whose diameter increases with the dispersed phase velocity detaches in the jetting regime. When the Bond number is above the critical value, the monodisperse droplet is generated in the dripping regime again, but the droplet detachment is dominated by the buoyancy. Moreover, the generated droplet diameter in this stage is the same as that in dripping regime driven by interfacial tension. The conclusion indicates that a steady dripping regime could be constructed over the whole rotational frequency range by employing the microchannel flow resistance design. During the processing, droplet detachment is dominated by the buoyancy before achieving the critical Capillary number.

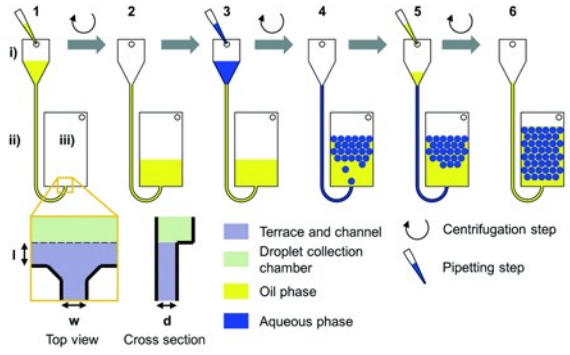

Fig. 7 Workflow of centrifugal step emulsification. The system is located on a spinning disk and consists of an inlet chamber (i), a channel (ii) which connects the inlet to a nozzle, and a droplet collection chamber (iii). Reproduced from Ref. 76 with permission from The Royal Society of Chemistry.

The schematic of the centrifugal step emulsification is shown in Fig. 7, which mainly includes a dispersed phase channel, a continuous reservoir, and a nozzle[76]. The continuous phase is injected into the reservoir first at a high rotational velocity, and then the dispersed phase crosses the step to form droplets by step emulsification mechanism with a suitable rotational velocity. In the process of droplet formation, centrifugal step emulsification drives the input of the dispersed phase and the backflow of the continuous phase synchronously under the influence of the centrifugal force. Simplified fluid control is an advantage compared with pressure-driven step emulsification. In addition, the density difference between the two phases favors removing the droplets from the nozzle exit dominated by the buoyancy; In this way, droplet merging and clustering are prevented spontaneously. Except for the nozzle height, the droplet size related to the buoyancy and the flow rate at the step junction are studied[77]. Combining efficient fluid delivery and monodisperse droplet formation, centrifugal step emulsification as an integrated system is suitable for the digital assays of biological samples.

An integrated centrifugal step emulsification device is designed for the absolute quantification of nucleic acids in recombinase polymerase amplification (RPA)[76]. The device is fabricated by micro-milling of PMMA, and parallel nozzles are provided for throughput enhancement, as shown in Fig. 8a. The droplet diameter produced by the device ranges from 120 to 170 μm with the CV remains between 2% and 4%. The linear relationship between the droplet diameter and nozzle height is observed in the experiments. Based on the structure, an advanced integrated step emulsification device is presented for the application of the digital droplet polymerase chain reaction (PCR)[78]. There is a tapered region in the continuous phase reservoir, through which the gas bubbles generated by degassing during thermal cycling could be transported from the detection region by a capillary driving mechanism. As shown in Fig. 8b. The device is fabricated by micro-milling the PMMA master, and the master is turned into a PDMS template; Then heat transfer the template into a COC device. It is confirmed that a tapered structure with inclination angles from 2° to 6° is effective for removing gas bubbles. Droplets with diameters of 147 μm are produced as the independent reaction and detection units in digital PCR. Another similar centrifugal step emulsification device is used for the absolute quantification of nucleic acids in digital droplet loop-mediated isothermal amplification (ddLAMP)[79], as shown in Fig. 8c. Furthermore, to improve the internal volume fraction, which is defined as the volume of the dispersed phase relative to the total emulsion volume, a tree type microchannel was designed for centrifugal step emulsification[80], as shown in Fig. 8d.

View Article Online
DOI: 10.1039/D0CC03628E

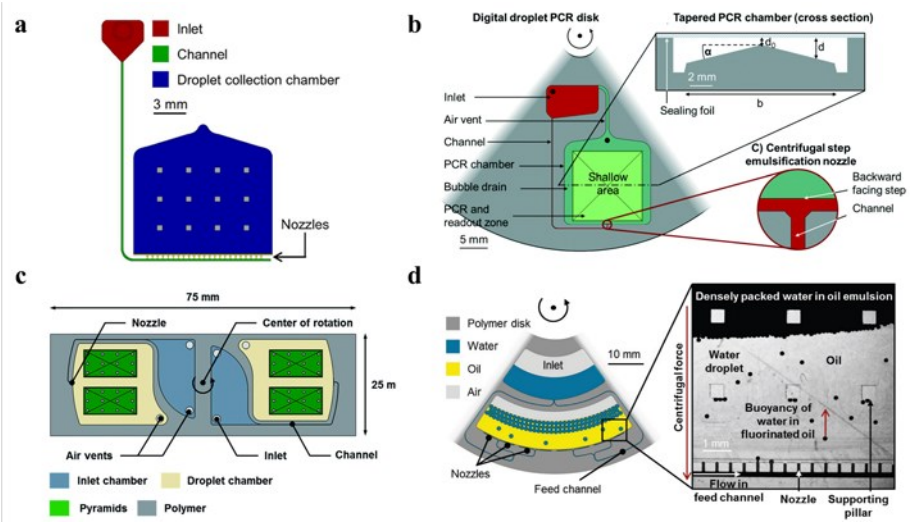

Fig. 8 Schematic of the centrifugal step emulsification. (a) Schematic of the centrifugal step emulsification with 23 parallel nozzles. [Ref. 76] - Published by The Royal Society of Chemistry. (b) Schematic of the centrifugal step emulsification with a tapered reservoir for digital droplet PCR on disk. [Ref. 78] - Published by The Royal Society of Chemistry. (c) Centrifugal DropChip for ddLAMP. [Ref. 79] - Published by The Royal Society of Chemistry. (d) Centrifugal step emulsification with a tree-typed microchannel.[80]

5. Conclusion and perspective

5.1 Step emulsification for specific applications

Microchannel confinement inducing droplet formation leads to the obvious advantages of droplet homogeneity and throughput, which also limits the flexibility in the practice of step emulsification.

First, in step emulsification, the monodisperse droplet size is related to the geometric characterizations of the microchannel and independent of the flow rates of the fluids in the dripping regime, which means that the droplet diameter is difficult to adjust once the microchannel is designed. In contrast, droplet microfluidic technologies such as T-junction, flow focusing, and co-flowing could adjust the droplet size through controlling the velocity of the fluids. There is no doubt that generating droplets with required diameters could greatly expand the application scope of a single device, which is one of the reasons why such structures have been widely applied commercially. Second, the payloads of single droplets are difficult to control in step emulsification compared with other methods[81-83]. Considering the systematic complexity and experimental efficiency, researchers usually configure the reagents in advance and then inject them as the dispersed phase into the microchannel to form monodisperse droplets. Hence, payloads such as the reagent type, concentration, and ratio, etc. have been determined before droplets are generated. Third, step emulsification is difficult to expand as a platform for multiple emulsions. Due to the inherent 3D structure, it is impractical to realize multiple emulsification through series structures similar to others[10, 84, 85].

As a result, based on the consideration of the structure flexibility, step emulsification is difficult to expand as a general droplet microfluidic platform for experiments. This method is more suitable for focusing on the high-throughput generation of monodisperse droplets with expected size and payload. Combined with biology, chemistry, medicine, sensing, and information technologies, step emulsification can have significant advantages in specific applications.

5.2 A data-driven model is effective

Although there are a large number of excellent experimental and theoretical analyses studying the mechanism of droplet formation in step emulsification, semiquantitative conclusions relying on experience are usually used for device design. Most of the mechanistic studies of droplet formation in step emulsification are based on some specific parameters of a specific structure. However, such studies do not sufficiently reflect the uniform and specific influences of the main physical parameters affecting the step emulsification among the various structures. Distinguishing the major and negligible parameters of step emulsification and finding the correlations between them and droplet formation may be more effective for experimental designs.

Data-driven machine learning models have the potential to characterize the mechanisms of step emulsification. With the development of information technology, machine learning has played a very important role in droplet microfluidics[86, 87], including biochemical experiments[88, 89] and droplet detection[90, 91]. Compared with traditional fluid simulation analysis models, machine learning models have advantages in finding the principal components among various parameters and characterizing their correlations in a complex nonlinear system. Based on a sufficient amount of representative data, it may be feasible to quantify the strong correlations between various parameters in step emulsification.

5.3 Fabrication is available

For the fabrication of step emulsification microchannels, the current mainstream sizes are at the micron level. Combining an affordable cost and acceptable precision, soft lithography is the most popular technique in microfluidic manufacturing. In step

emulsification, soft lithography is usually used to fabricate a SU-8 master with a structure height higher than 20 μm. Considering that the aspect ratio of the nozzle is not significantly high in most cases, the technique is feasible for channel heights down to 2 μm. However, due to planar processing, as the channel size becomes increasingly meticulous, the overlay alignment of multilayer structures to form the height difference of the step emulsification microchannels is increasingly difficult. In addition, the problems of the common material PDMS, such as deformation and swelling, should be sufficiently considered in practical applications.

Deep reactive ion etching (DRIE) is one of the most popular dry etching technologies in micro-manufacturing. This technique is suitable for the fabrication of high aspect-ratio (up to 30)[92] structures. In step emulsification, DRIE with contact lithography is commonly used for fabrications with channel depths from 1 μm to 20 μm. To generate droplets with smaller sizes, DRIE is still applicable to nanochannels. With projection and electron beam lithography, DRIE could realize nanochannels fabrication with minimum sizes of 90 nm and 10 nm, respectively. Although DRIE has extremely high fabrication performance for silicon wafers, it is not suitable for the precise processing of other substrate materials, such as glass, quartz, and metal. In addition, the cost of DRIE is much higher than that of soft lithography and increases significantly with fabrication precision.

High-precision 3D printing technology has the technical advantages of 3D manufacturing, which is exactly what step emulsification requires. Although the accuracy has been sufficient to meet the requirements of microchannels, such a technology has not been fully utilized in step emulsification[67]. As far as we know, 3D printing technology with 10 μm precision is suitable for microchannel fabrication greater than 50um width and 10 μm depth. For higher accuracy requirements, 3D printing with 2 μm precision could fabricate a minimum channel size with a 10 μm width and 5um depth[93-95]. Nonetheless, the limitation of available materials still exists, which commonly include kinds of resins. In addition, 3D printing does not have the cost and efficiency advantages of batch generation. Although such limitations should be considered in practice, 3D processing capability, sufficient accuracy, and acceptable cost would make high-precision 3D printing technology more widely used in the fabrication of step emulsification devices.

5.4 There are many rooms in digital detection

Step emulsification has been efficiently applied in biomaterial synthesis and digital assays, such as digital PCR, digital LAMP, and single-cell detection. In practical applications, step emulsification combined with sensing and detection technology will play an important role in point-of-care testing (POCT), and further development towards integration and portability is needed.

First, the control of the fluid drive should be simpler. The complex equipment and operations of the fluidic drive hinder step emulsification from going out of the laboratory. Centrifugal step emulsification based on a conventional centrifuge is a direction for integration. The solutions include generating and storing monodisperse droplets within a microfluidic chip[96, 97] and emulsification in a centrifuge tube[98-100], which promotes step emulsification towards integration and portability respectively. More novel step emulsification structures with simple fluid operation need to be explored to match the integrated and portable detections.

Second, to meet the actual POCT applications, it is necessary to break through the droplet flexibility limitation of step emulsification. Both the droplet diameter and throughput need to be adjusted in a certain range for a single device. To address this requirement, modular microfluidics[101] can potentially be applied to portable devices combining with step emulsification. When the channels cannot be changed for a fixed structure, different components of step emulsification structure could be replaced through modular conversion to adjust the droplet diameter and throughput.

Third, the digital detection technologies are to be expanded. At present, droplet detection is mainly based on the fluorescence signal of the reaction products, including flow-based fluorescent detection and image-based fluorescent detection[102-104]. A direction towards portable POCT is optofluidic platforms combining step emulsification with smartphones[105-107]. Due to the extremely high droplet flux in digital assays, more imaging solutions and artificial intelligence algorithms based on smartphones would help to realize the integration of the emulsification, reaction, imaging, calculation, and visualization. Furthermore, integrating high-performance biosensors would expand the detection from fluorescence signals and contribute to improving the specificity, sensitivity, and systematic integration[108]. Combined with biochemical and optoelectronic technologies, such step emulsification digital platforms would expand the fluorescent, colorimetric, chemiluminescent, electrochemical measurements, etc. into dispersed.

We believe that step emulsification, as a robust platform for discretizing samples, combined with sensing, detection, and information technologies will open up more space for bioinformation measurement.

Conflicts of interest

There are no conflicts to declare.

Acknowledgments

This work is supported by the National Key R&D Program of China (Nos. 2018YFE0205000 and 2017YFA0205103), the National Natural Science Foundation of China (No. 81571766), the Natural Science Foundation of Tianjin (No. 17JCYBJC24400), and the 111 Project of China (No. B07014).

References

1 A. A. Maan, A. Nazir, M. K. I. Khan, R. Boom and K. Schroën, *Journal of Food Engineering*, 2015, **147**, 1-7.
2 B. Wang, P. Prinsen, H. Wang, Z. Bai, H. Wang, R. Luque and J. Xuan, *Chem Soc Rev*, 2017, **46**, 855-914.

3 Y. Chao and H. C. Shum, *Chem Soc Rev*, 2020, **49**, 114-142.
4 Y. Ding, P. D. Howes and A. J. deMello, *Analytical Chemistry*, 2020, **92**, 132-149.
5 A. Suea-Ngam, P. D. Howes, M. Srisa-Art and A. J. deMello, *Chem Commun*, 2019, **55**, 9895-9903.
6 W. Li, L. Zhang, X. Ge, B. Xu, W. Zhang, L. Qu, C.-H. Choi, J. Xu, A. Zhang, H. Lee and D. A. Weitz, *Chem Soc Rev*, 2018, **47**, 5646-5683.
7 Y. K. Jo and D. Lee, *SMALL*, 2019, **16**, 03736.
8 Z. H. Liu, F. Fontana, A. Python, J. T. Hirvonen and H. A. Santos, *Small*, 2020, **16**.
9 J. Nette, P. D. Howes and A. J. deMello, *Advanced Materials Technologies*, 2020.
10 T. Y. Lee, T. M. Choi, T. S. Shim, R. A. M. Frijns and S.-H. Kim, *LAB ON A CHIP*, 2016, **16**, 3415-3440.
11 M. G. Bah, H. M. Bilal and J. Wang, *Soft Matter*, 2020, **16**, 570-590.
12 C.-X. Zhao, *Advanced Drug Delivery Reviews*, 2013, **65**, 1420-1446.
13 F. He, M.-J. Zhang, W. Wang, Q.-W. Cai, Y.-Y. Su, Z. Liu, Y. Faraj, X.-J. Ju, R. Xie and L.-Y. Chu, *ADVANCED MATERIALS TECHNOLOGIES*, 2019, **4**.
14 W. W. Chen, F. C. Shao and Y. L. Xianyu, *Small*, 2020, **16**.
15 E. M. Payne, D. A. Holland-Moritz, S. Sun and R. T. Kennedy, *Lab on a Chip*, 2020, **20**, 2247-2262.
16 T. S. Kaminski and P. Garstecki, *Chem Soc Rev*, 2017, **46**, 6210-6226.
17 B. J. Hindson, K. D. Ness, D. A. Masquelier, P. Belgrader, N. J. Heredia, A. J. Makarewicz, I. J. Bright, M. Y. Lucero, A. L. Hiddessen, T. C. Legler, T. K. Kitano, M. R. Hodel, J. F. Petersen, P. W. Wyatt, E. R. Steenblock, P. H. Shah, L. J. Bousse, C. B. Troup, J. C. Mellen, D. K. Wittmann, N. G. Erndt, T. H. Cauley, R. T. Koehler, A. P. So, S. Dube, K. A. Rose, L. Montesclaros, S. Wang, D. P. Stumbo, S. P. Hodges, S. Romine, F. P. Milanovich, H. E. White, J. F. Regan, G. A. Karlin-Neumann, C. M. Hindson, S. Saxonov and B. W. Colston, *Analytical Chemistry*, 2011, **83**, 8604-8610.
18 W. W. Liu, Y. Zhu, Y. M. Feng, J. Fang and Q. Fang, *Analytical Chemistry*, 2017, **89**, 822-829.
19 K. Matula, F. Rivello and W. T. S. Huck, *Advanced Biosystems*, 2020, **4**.
20 L. Mazutis, J. Gilbert, W. L. Ung, D. A. Weitz, A. D. Griffiths and J. A. Heyman, *NATURE PROTOCOLS*, 2013, **8**, 870-891.
21 D. Hess, T. Yang and S. Stavrakis, *Analytical and bioanalytical chemistry*, 2019, **412**, 3265–3283.
22 R. Arayanarakool, L. Shui, S. W. M. Kengen, A. van den Berg and J. C. T. Eijkel, *LAB ON A CHIP*, 2013, **13**, 1955-1962.
23 F. Lan, B. Demaree, N. Ahmed and A. R. Abate, *Nat Biotechnol*, 2017, **35**, 640–646.
24 M. Rhee, Y. K. Light, R. J. Meagher and A. K. Singh, *Plos One*, 2016, **11**, e0153699.
25 P. Zhu and L. Wang, *LAB ON A CHIP*, 2017, **17**, 34-75.
26 T. Thorsen, R. W. Roberts, F. H. Arnold and S. R. Quake, *Physical Review Letters*, 2001, **86**, 4163-4166.
27 T. Nisisako and T. Torii, *Lab on a Chip*, 2008, **8**, 287-293.
28 H. Peng, M. Zhu, Z. Gao, C. Liao, C. Jia, H. Wang, H. Zhou and J. Zhao, *Biomedical Microdevices*, 2020, **22**.
29 W. B. Han and X. Y. Chen, *Microgravity Sci Tec*, 2019, **31**, 855-864.
30 W. B. Han and X. Y. Chen, *Chem Eng Res Des*, 2019, **145**, 213-225.
31 P. B. Umbanhowar, V. Prasad and D. A. Weitz, *Langmuir*, 2000, **16**, 347-351.
32 A. S. Utada, L. Y. Chu, A. Fernandez-Nieves, D. R. Link, C. Holtze and D. A. Weitz, *MRS Bulletin*, 2007, **32**, 702-708.
33 B. Haney, D. Chen, L.-H. Cai, D. Weitz and S. Ramakrishnan, *Langmuir*, 2019, **35**, 4693-4701.
34 S. L. Anna, N. Bontoux and H. A. Stone, *Applied Physics Letters*, 2003, **82**, 364-366.
35 L. Yobas, S. Martens, O. Wee-Liat and N. Ranganathan, *Lab on a Chip*, 2006, **6**, 1073-1079.
36 T. D. Rane, C. Liben, H. C. Zec and W. Tza-Huei, *Lab on a Chip*, 2015, **15**, 776-782.
37 W. B. Han, X. Y. Chen, Z. L. Wu and Y. Zheng, *J Braz Soc Mech Sci*, 2019, **41**, 265.
38 T. Kawakatsu, Y. Kikuchi and M. Nakajima, *JAOCS, Journal of the American Oil Chemists' Society*, 1997, **74**, 317-321.
39 I. Chakraborty, J. Ricouvier, P. Yazhgur, P. Tabeling and A. M. Leshansky, *Lab on a Chip*, 2017, **17**, 3609-3620.
40 Z. Li, A. M. Leshansky, S. Metais, L. M. Pismen and P. Tabeling, *Lab on a Chip*, 2015, **15**, 3095-3095.
41 G. T. Vladisavljevic, E. E. Ekanem, Z. L. Zhang, N. Khalid, I. Kobayashi and M. Nakajima, *Chem Eng J*, 2018, **333**, 380-391.
42 S. Sugiura, M. Nakajima and M. Seki, *Langmuir*, 2002, **18**, 3854-3859.
43 S. Sugiura, M. Nakajima and M. Seki, *Langmuir*, 2002, **18**, 5708-5712.
44 K. C. Van Dijke, K. C. P. G. Schroen and R. M. Boom, *Langmuir*, 2008, **24**, 10107-10115.
45 I. Kobayashi, G. T. Vladisavljevic, K. Uemura and M. Nakajima, *Chem Eng Sci*, 2011, **66**, 5556-5565.
46 E. Van Der Zwan, K. Schroen and R. Boom, *Langmuir*, 2009, **25**, 7320-7327.
47 R. Dangla, E. Fradet, Y. Lopez and C. N. Baroud, *J Phys D Appl Phys*, 2013, **46**, 114003.
48 R. Dangla, S. C. Kayi and C. N. Baroud, *Proc Natl Acad Sci U S A*, 2013, **110**, 853-858.
49 P. Garstecki, H. A. Stone and G. M. Whitesides, *Physical Review Letters*, 2005, **94**, 164501-164501.
50 N. Mittal, C. Cohen, J. Bibette and N. Bremond, *Phys Fluids*, 2014, **26**, 082109.
51 A. Montessori, M. Lauricella, S. Succi, E. Stolovicki and D. Weitz, *Phys Rev Fluids*, 2018, **3**, 072202.
52 S. Sugiura, M. Nakajima, S. Iwamoto and M. Seki, *Langmuir*, 2001, **17**, 5562-5566.
53 S. Sugiura, M. Nakajima, N. Kumazawa, S. Iwamoto and M. Seki, *Journal of Physical Chemistry B*, 2002, **106**, 9405-9409.
54 S. Sugiura, M. Nakajima, T. Oda, M. Satake and M. Seki, *Journal of Colloid and Interface Science*, 2004, **269**, 178-185.
55 I. Kobayashi, S. Mukataka and M. Nakajima, *Langmuir*, 2004, **20**, 9868-9877.
56 K. van Dijke, R. de Ruiter, K. Schroen and R. Boom, *Soft Matter*, 2010, **6**, 321-330.
57 K. Van Dijke, I. Kobayashi, K. Schroen, K. Uemura, M. Nakajima and R. Boom, *Microfluidics and Nanofluidics*, 2010, **9**, 77-85.
58 A. A. Maan, K. Schroen and R. Boom, *Microfluidics and Nanofluidics*, 2013, **14**, 187-196.
59 I. Kobayashi, S. Mukataka and M. Nakajima, *Langmuir*, 2005, **21**, 5722-5730.
60 M. Wang, C. Kong, Q. Liang, J. X. Zhao, M. L. Wen, Z. B. Xu and X. D. Ruan, *Rsc Adv*, 2018, **8**, 33042-33047.
61 J. Y. Lian, X. Y. Luo, X. Huang, Y. H. Wang, Z. B. Xu and X. D. Ruan, *Colloid Surface A*, 2019, **568**, 381-390.
62 J. Y. Lian, S. X. Zheng, C. Liu, Z. B. Xu and X. D. Ruan, *Colloid Surface A*, 2019, **580**.
63 I. Kobayashi, M. Nakajima, K. Chun, Y. Kikuchi and H. Fujita, *AIChE Journal*, 2002, **48**, 1639-1644.
64 I. Kobayashi, M. Nakajima and S. Mukataka, *Colloids and Surfaces A: Physicochemical and Engineering Aspects*, 2003, **229**, 33-41.
65 I. Kobayashi, S. Mukataka and M. Nakajima, *Journal of Colloid and Interface Science*, 2004, **279**, 277-280.
66 I. Kobayashi, S. Mukataka and M. Nakajima, *Industrial and Engineering Chemistry Research*, 2005, **44**, 5852-5856.

67 E. Stolovicki, R. Ziblat and D. A. Weitz, *Lab on a Chip*, 2018, **18**, 132-138.
68 K. van Dijke, G. Veldhuis, K. Schroen and R. Boom, *Lab on a Chip*, 2009, **9**, 2824-2830.
69 S. Sahin and K. Schroen, *Lab on a Chip*, 2015, **15**, 2486-2495.
70 A. S. Opalski, K. Makuch, Y. K. Lai, L. Derzsi and P. Garstecki, *Lab on a Chip*, 2019, **19**, 1183-1192.
71 E. Amstad, M. Chemama, M. Eggersdorfer, L. R. Arriaga, M. P. Brenner and D. A. Weitz, *Lab on a Chip*, 2016, **16**, 4163-4172.
72 A. Ofner, D. G. Moore, P. A. Ruhs, P. Schwendimann, M. Eggersdorfer, E. Amstad, D. A. Weitz and A. R. Studart, *Macromolecular Chemistry and Physics*, 2017, **218**, 1600472.
73 F. Dutka, A. S. Opalski and P. Garstecki, *Lab on a Chip*, 2016, **16**, 2044-2049.
74 A. G. Hati, T. R. Szymborski, M. Steinacher and E. Amstad, *Lab on a Chip*, 2018, **18**, 648-654.
75 M. Schulz, F. von Stetten, R. Zengerle and N. Paust, *Langmuir*, 2019, **35**, 9809-9815.
76 F. Schuler, F. Schwemmer, M. Trotter, S. Wadle, R. Zengerle, F. von Stetten and N. Paust, *Lab on a Chip*, 2015, **15**, 2759-2766.
77 L. Clime, L. Malic, J. Daoud, L. Lukic, M. Geissler and T. Veres, *Lab on a Chip*, 2020, DOI: 10.1039/D0LC00333F.
78 F. Schuler, M. Trotter, M. Geltman, F. Schwemmer, S. Wadle, E. Dominguez-Garrido, M. Lopez, C. Cervera-Acedo, P. Santibanez, F. von Stetten, R. Zengerle and N. Paust, *Lab on a Chip*, 2016, **16**, 208-216.
79 F. Schuler, C. Siber, S. Hin, S. Wadle, N. Paust, R. Zengerle and F. Von Stetten, *Anal Methods-Uk*, 2016, **8**, 2750-2755.
80 F. Schuler, N. Paust, R. Zengerle and F. von Stetten, *Micromachines*, 2015, **6**, 1180-1188.
81 F. Zhang, L. Jiang, C. Zeng, C. Wang, J. Wang, X. Ke and L. Zhang, *Soft Matter*, 2020, **16**, 5981-5989.
82 L. Y. Zhang, K. W. Chen, H. Y. Zhang, B. Pang, C. H. Choi, A. S. Mao, H. B. Liao, S. Utech, D. J. Mooney, H. N. Wang and D. A. Weitz, *Small*, 2018, **14**, 1702955.
83 T. Trantidou, M. S. Friddin, A. Salehi-Reyhani, O. Ces and Y. Elani, *Lab on a Chip*, 2018, **18**, 2488-2509.
84 M. Azarmanesh, S. Bawazeer, A. A. Mohamad and A. Sanati-Nezhad, *Sci Rep-Uk*, 2019, **9**.
85 S. S. Terekhov, I. V. Smirnov, A. V. Stepanova, T. V. Bobik, Y. A. Mokrushina, N. A. Ponomarenko, A. A. Belogurov, M. P. Rubtsova, O. V. Kartseva, M. O. Gomzikova, A. A. Moskovtsev, A. S. Bukatin, M. V. Dubina, E. S. Kostryukova, V. V. Babenko, M. T. Vakhitova, A. I. Manolov, M. V. Malakhova, M. A. Kornienko, A. V. Tyakht, A. A. Vanyushkina, E. N. Ilina, P. Masson, A. G. Gabibov and S. Altman, *P Natl Acad Sci USA*, 2017, **114**, 2550-2555.
86 J. W. Khor, N. Jean, E. S. Luxenberg, S. Ermon and S. K. Y. Tang, *Soft Matter*, 2019, **15**, 1361-1372.
87 C. M. Svensson, O. Shvydkiv, S. Dietrich, L. Mahler, T. Weber, M. Choudhary, M. Tovar, M. T. Figge and M. Roth, *Small*, 2019, **15**, 1802384.
88 J. Riordon, D. Sovilj, S. Sanner, D. Sinton and E. W. K. Young, *Trends Biotechnol*, 2019, **37**, 310-324.
89 S. Sarkar, W. Kang, S. Jiang, K. Li, S. Ray, E. Luther, A. R. Ivanov, Y. Fu and T. Konry, *Lab on a Chip*, 2020, **20**, 2317-2327.
90 A. Arjun, R. R. Ajith and S. K. Ranjith, *Biomicrofluidics*, 2020, **14**, 034111.
91 P. Hadikhani, N. Borhanil, S. M. H. Hashemi and D. Psaltis, *Sci Rep-Uk*, 2019, **9**.
92 J. Yeom, Y. Wu, J. C. Selby and M. A. Shannon, *J Vac Sci Technol B*, 2005, **23**, 2319-2329.
93 Z. Chai, M. Liu, L. Chen, Z. L. Peng and S. H. Chen, *Soft Matter*, 2019, **15**, 8879-8885.
94 L. Xiao, G. Li, Y. Cai, Z. Cui, J. Fang, H. Cheng, Y. Zhang, T. Duan, H. Zang, H. Liu, S. Li, Z. Ni and Y. Hu, *Chem Eng J*, 2020, **399**, 125139.
95 S. Feng, J. Delannoy, A. Malod, H. Zheng, D. Quéré and Z. Wang, *Sci Adv*, 2020, **6**, eabb4540.
96 X. R. Li, D. F. Zhang, W. D. Ruan, W. Z. Liu, K. Yin, T. Tian, Y. P. Bi, Q. Y. Ruan, Y. Zhao, Z. Zhu and C. Y. Yang, *Analytical Chemistry*, 2019, **91**, 13611-13619.
97 M. Schulz, S. Calabrese, F. Hausladen, H. Wurm, D. Drossart, K. Stock, A. M. Sobieraj, F. Eichenseher, M. J. Loessner, M. Schmelcher, A. Gerhardts, U. Goetz, M. Handel, A. Serr, G. Haecker, J. Li, M. Specht, P. Koch, M. Meyer, P. Tepper, R. Rother, M. Jehle, S. Wadle, R. Zengerle, F. von Stetten, N. Paust and N. Borst, *Lab on a Chip*, 2020, **20**, 2549-2561.
98 M. Schulz, S. Probst, S. Calabrese, A. R. Homann, N. Borst, M. Weiss, F. von Stetten, R. Zengerle and N. Paust, *Molecules*, 2020, **25**.
99 D. C. Shin, Y. Morimoto, J. Sawayama, S. Miura and S. Takeuchi, *Sensor Actuat B-Chem*, 2019, **301**, 034111.
100 Z. T. Chen, P. Y. Liao, F. L. Zhang, M. C. Jiang, Y. S. Zhu and Y. Y. Huang, *Lab on a Chip*, 2017, **17**, 235-240.
101 X. Lai, Z. Shi, Z. Pu, P. Zhang, X. Zhang, H. Yu and D. Li, *Microsystems & Nanoengineering*, 2020, **6**, 27.
102 Z. A. Hu, F. J. Xu, G. W. Sun, S. C. Zhang and X. R. Zhang, *Chem Commun*, 2020, **56**, 5409-5412.
103 T. J. Abram, H. Cherukury, C. Y. Ou, T. Vu, M. Toledano, Y. Y. Li, J. T. Grunwald, M. N. Toosky, D. F. Tifrea, A. Slepenkin, J. Chong, L. S. Kong, D. V. Del Pozo, K. T. La, L. Labanieh, J. Zimak, B. Shen, S. S. Huang, E. Gratton, E. M. Peterson and W. A. Zhao, *Lab on a Chip*, 2020, **20**, 477-489.
104 S. B. Tian, Z. Zhang, J. Y. Chen, M. Y. Du, Z. Li, H. Yang, X. H. Ji and Z. K. He, *Talanta*, 2018, **186**, 24-28.
105 V. Yelleswarapu, J. R. Buser, M. Haber, J. Baron, E. Inapuri and D. Issadore, *P Natl Acad Sci USA*, 2019, **116**, 4489-4495.
106 H. Xu, A. Y. Xia, D. D. Wang, Y. H. Zhang, S. L. Deng, W. P. Lu, J. Luo, Q. Zhong, F. L. Zhang, L. Zhou, W. Q. Zhang, Y. Wang, C. Yang, K. Chang, W. L. Fu, J. H. Cui, M. Z. Gan, D. Luo and M. Chen, *Sci Adv*, 2020, **6**, 2375-2548.
107 V. R. Yelleswarapu, H. H. Jeong, S. Yadavali and D. Issadore, *Lab on a Chip*, 2017, **17**, 1083-1094.
108 R. G. Mahmudunnabi, F. Z. Farhana, N. Kashaninejad, S. H. Firoz, Y.-B. Shim and M. J. A. Shiddiky, *Analyst*, 2020, **145**, 4398-4420.